Distribution of zeros of the Husimi function in systems with degeneracy

I. Oregi and F. J. Arranz*
Grupo de Sistemas Complejos, Universidad Politécnica de Madrid, 28040 Madrid, Spain
(Received 9 December 2013; published 10 February 2014)

The distribution of zeros of the Husimi function of energy eigenstates has proven to be a very useful tool for the characterization of the quantum transition from order to chaos in systems without degeneracy. In this paper, we show, by means of calculations on the Hénon-Heiles Hamiltonian system, that the quantum order-chaos transition in systems with degeneracy can also be characterized through the distribution of the Husimi function zeros, providing that the appropriate linear combination of degenerate eigenstates is used. If using an arbitrary linear combination, spurious results can be achieved, suggesting a wrong premature quantum transition to chaos.

DOI: 10.1103/PhysRevE.89.022909 PACS number(s): 05.45.Mt, 05.45.Ac, 03.65.Sq

I. INTRODUCTION

In the seminal paper of Lebœuf and Voros [1], the distribution of zeros of the Husimi function was shown as a meaningful indicator of the regular or chaotic character of an energy eigenstate from a quantum map. Specifically, the distribution of zeros is one dimensional, the zeros being distributed along a line, for regular eigenstates, while it is two dimensional, with the zeros spreading out in Husimi phase space, for chaotic eigenstates.

Thereafter, different studies have extended the properties of the distributions of zeros in quantum maps [2–4], and also these properties have been established in more realistic systems. Thus, the regular or chaotic behavior of the quantum states has been characterized through the distributions of the Husimi zeros in the spin-boson interaction model [5,6], in quantum billiards [7,8], in one-dimensional autonomous (therefore integrable) systems [9,10], in spin Stern-Gerlach apparatus [11] (where the possibility of experimental measurement of the zeros by means of a Stern-Gerlach apparatus is shown), in acoustic waveguides [12], and also in molecular systems [13–16].

Nevertheless, in all these studies only nondegenerate energy eigenstates have been regarded, so that the behavior of the distributions of Husimi zeros of degenerate eigenstates remains unknown. In the present work, the behavior of the Husimi zeros of degenerate eigenstates in the order-chaos transition is examined by means of calculations on a well known system with degeneracy: the Hénon-Heiles Hamiltonian system.

The Hénon-Heiles system is a paradigmatic chaotic system, initially proposed by Hénon and Heiles as a model for galactic motion [17], and widely used thereafter in the study of different features of nonlinear dynamical systems. Thus, recent works resort to the Hénon-Heiles Hamiltonian for studying generalized bifurcation diagrams in conservative systems [18], the amplitude death phenomena in delay-coupled Hamiltonian systems [19], the symmetry properties of orthogonal and covariant Lyapunov vectors and their exponents [20], the weakly noisy chaotic scattering [21], and the second-order normal forms of Hamiltonian systems relative to periodic flows [22].

The organization of the paper is as follows. In Sec. II the Hénon-Heiles Hamiltonian and also the performed classical and quantum calculations are described. Next, the obtained results are presented and discussed in Sec. III. Finally, the conclusions are summarized in Sec. IV.

II. SYSTEM DESCRIPTION AND CALCULATIONS

A. The Hénon-Heiles Hamiltonian

The Hénon-Heiles system [17] is defined by means of the Hamiltonian function

$$H = \frac{1}{2}\left(p_x^2 + p_y^2\right) + \frac{\omega^2}{2}(x^2 + y^2) + \frac{\lambda}{3}(3x^2 y - y^3), \quad (1)$$

where (x, y, p_x, p_y) are Cartesian coordinates and its conjugated momenta, $\omega > 0$ is the harmonic frequency, and $\lambda > 0$ the chaos parameter. Notice that the Hamiltonian in Eq. (1) tends to the (integrable) isotropic harmonic oscillator as $\lambda \to 0$, leading to a separable in (x, p_x) and (y, p_y) coordinates Hamiltonian function $H_0 = H_{0x} + H_{0y}$, with two motion constants corresponding to the energy for each Cartesian degree of freedom, $E_x = H_{0x}$ and $E_y = H_{0y}$.

The Hénon-Heiles system can also be expressed in polar coordinates $(r, \theta, p_r, p_\theta)$ by using the canonical transformation

$$\begin{aligned} r &= +\sqrt{x^2 + y^2}, \quad & p_r &= (x p_x + y p_y)/(x^2 + y^2), \\ \theta &= \arctan(y/x), \quad & p_\theta &= x p_y - y p_x, \end{aligned} \quad (2)$$

leading to the following Hamiltonian function:

$$H' = \frac{1}{2}\left(p_r^2 + \frac{p_\theta^2}{r^2}\right) + \frac{\omega^2}{2} r^2 + \frac{\lambda}{3} r^3 \sin(3\theta). \quad (3)$$

Note that, at the integrable limit $\lambda \to 0$, the Hamiltonian in Eq. (3) has two motion constants: the total energy $E = H_0'$ and the angular momentum p_θ (indeed, for $\lambda = 0$ the coordinate θ is cyclic).

As can be observed in Fig. 1, the potential energy function of the Hénon-Heiles system $V(x, y)$ has a minimum at the origin, where $V(0,0) = 0$, and three symmetric saddle points at $(x_s, y_s) = (0,1), (\pm\sqrt{3}/2, -1/2)$ in ω^2/λ units, where $E_s \equiv V(x_s, y_s) = \omega^6/6\lambda^2$. For a total energy below the saddle points energy E_s, the system is classically bounded. In this work, we will focus on the bounded region of the potential energy surface.

*fj.arranz@upm.es

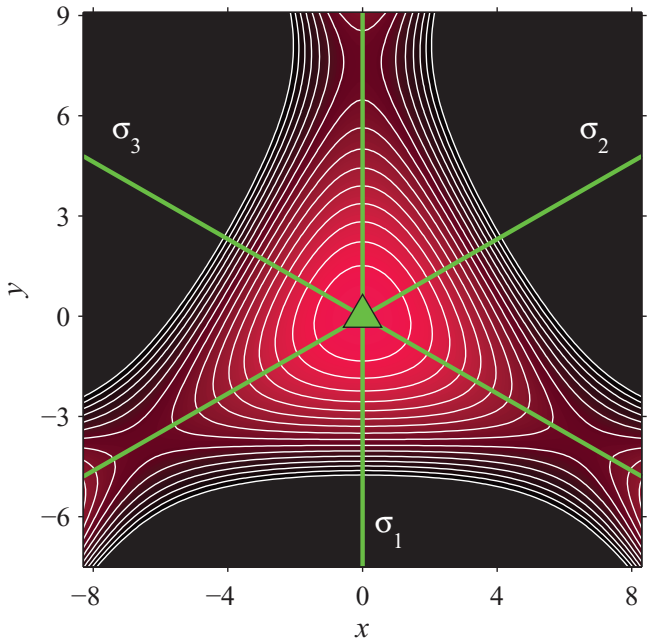

FIG. 1. (Color online) Potential energy function V of the Hénon-Heiles system, with parameter values $\omega = 1$ and $\lambda = \sqrt{0.0175}$, depicted as contour lines spaced one unit from $V = 0$ to $V = 16$. The symmetry elements corresponding to the C_{3v} point group have been also represented: the ternary axis C_3 (△), and the three vertical planes σ_1, σ_2, and σ_3 (thick line).

The concavity-convexity analysis of Toda [23] applied to the Hénon-Heiles system leads to the order-chaos circular boundary $r_b = \omega^2/2\lambda$, which is reached at the threshold energy $E_b = \omega^6/12\lambda^2$. Observe that the threshold energy E_b is exactly half of the escape energy E_s.

In addition, the Hénon-Heiles potential belongs to the C_{3v} (Schönflies notation) symmetry point group, whose symmetry elements, the ternary axis C_3 and the three vertical planes σ_1, σ_2, and σ_3, are represented in Fig. 1. Note that the C_{3v} symmetry of the Hénon-Heiles potential is shown clearly in the polar representation in Eq. (3).

B. Classical calculations

The Hamilton equations of motion corresponding to Eq. (1) with parameter values $\omega = 1$ and $\lambda = \sqrt{0.0175}$ have been built, and standard numerical integration has been used to obtain solution trajectories for the Hénon-Heiles system. In order to get a suitable graphical representation of the phase space structure, we have calculated composite Poincaré surfaces of section (PSSs) on a symmetry plane for increasing energies up to the saddle points energy $E_s = 9.524$.

For this purpose, the symmetry plane σ_1 has been used by making $x = 0$, and the positive value of momentum $p_x > 0$ chosen, leading to the $(y, p_y)_E$ representation of the PSS for a total energy E. Notice that, due to symmetry constraints, a bounded trajectory in configuration space contained in a symmetry plane is necessarily periodic. Then, the motions along the σ planes correspond to periodic orbits (POs). Particularly, the symmetry plane σ_1 defining the PSS contains a PO, and this orbit does not cross the plane at $x = 0$ because it is contained in the plane. Thus, the representation of this PO on the PSS corresponds to the energy boundary, given by the condition $H(x = 0, y, p_x = 0, p_y) = E$ for a total energy E.

C. Quantum calculations

In order to obtain the Husimi functions, first the eigenenergies and quasibounded[1] eigenstates of the Hamiltonian operator corresponding to the Hamiltonian function in Eq. (1) (with parameter values $\omega = 1$, $\lambda = \sqrt{0.0175}$, and Planck's constant $\hbar = 0.5$) have been calculated, and then the corresponding Husimi functions obtained by means of a basis set change in Hilbert space.

The eigenenergies and eigenstates calculation has been performed by using a two-dimensional Gaussian basis set $\{\chi_k\}_{k=1}^N$, where

$$\chi_k(x,y) = \sqrt{\frac{2\alpha}{\pi}} e^{-\alpha[(x-x_k)^2+(y-y_k)^2]}, \tag{4}$$

distributed over a C_{3v} hexagonal grid at points (x_k, y_k), as in the calculations of Hamilton and Light [24], bounded by the energy contour corresponding to the saddle points energy $E_s = 9.524$, and leading to a basis set with $N = 6 \times 169$ Gaussian functions. The exponential parameter is set to $\alpha = -2\log(S_{max})/\ell^2$, where $S_{max} = 0.8$ and $\ell = 1/4$ are, respectively, the maximum overlap and the minimum length between Gaussian functions in the grid, thus optimizing the numerical linear dependence prevention.[2] The matrix representation of the Hamiltonian operator in the Gaussian basis set has been built and then diagonalized by using the LAPACK routine DSYEV [25]. In this way, the 140 low lying eigenstates $\langle xy|n\rangle$ $(n = 1, \ldots, 140)$ with its eigenenergies E_n converged to within 4×10^{-4} have been obtained. Notice that all eigenvectors calculated by means of the routine DSYEV are real.

As is well known, the C_{3v} symmetry of the potential energy function induces the same symmetry in the eigenstates, so that they must belong to one of the irreducible representations of the C_{3v} symmetry point group (Mulliken notation): A_1 (one dimensional), A_2 (one dimensional), or E (two dimensional). Note that the symmetry adapted hexagonal grid simplifies the irreducible representation assignment of the eigenstates, so it is only necessary to verify the symmetry relations between the appropriate expansion coefficients for each eigenstate, as did Hamilton and Light in Ref. [24].

Moreover, the Husimi function $\mathcal{H}(\bar{x}, \bar{y}, \bar{p}_x, \bar{p}_y)$ of the eigenstate $|n\rangle$ can be defined as the probability density in the

[1]Strictly speaking, the eigenstates of the Hénon-Heiles system are unbounded and therefore their eigenenergies are unquantized. However, there exists a measure zero subset of eigenstates which are localized into the well, with negligible amplitudes in the unbounded region except perhaps for eigenenergies near the escape energy or above it.

[2]Notice that the overlap between Gaussian basis functions is given by $\langle\chi_i, \chi_j\rangle = \exp\{-\frac{\alpha}{2}[(x_i - x_j)^2 + (y_i - y_j)^2]\}$, so that the parameter value $\alpha = -2\log(S_{max})/\ell^2$ ensures a maximum overlap $\langle\chi_i, \chi_j\rangle_{max} = \exp\{-\frac{\alpha}{2}\ell^2\} = S_{max}$.

coherent states $|\bar{x}\,\bar{p}_x\,\bar{y}\,\bar{p}_y\rangle$ representation

$$\mathcal{H}(\bar{x},\bar{y},\bar{p}_x,\bar{p}_y) = \frac{1}{(2\pi\hbar)^2}|\langle\bar{x}\,\bar{p}_x\,\bar{y}\,\bar{p}_y|n\rangle|^2, \tag{5}$$

where $\langle\bar{x}\,\bar{p}_x\,\bar{y}\,\bar{p}_y|n\rangle$ is calculated by means of the following basis set change in Hilbert space:

$$\langle\bar{x}\,\bar{p}_x\,\bar{y}\,\bar{p}_y|n\rangle = \int dx \int dy \langle\bar{x}\,\bar{p}_x\,\bar{y}\,\bar{p}_y|xy\rangle\langle xy|n\rangle, \tag{6}$$

being $\langle\bar{x}\,\bar{p}_x\,\bar{y}\,\bar{p}_y|xy\rangle$ the harmonic oscillator coherent packet given by

$$\langle\bar{x}\,\bar{p}_x\,\bar{y}\,\bar{p}_y|xy\rangle = \sqrt{\frac{\omega}{\pi\hbar}}e^{-\omega[(\bar{x}-x)^2+(\bar{y}-y)^2]/2\hbar} \times e^{i[(\bar{x}-2x)\bar{p}_x+(\bar{y}-2y)\bar{p}_y]/2\hbar}. \tag{7}$$

In order to get a suitable graphical representation, and to be able to compare with the classical calculations, a quantum Poincaré surface of section (QPSS) for the eigenenergy E_n, $\mathcal{H}_s(\bar{y},\bar{p}_y;E_n)$, based on the Husimi function has been calculated by setting, similarly to the classical PSS, $\bar{x}=0$ and $\bar{p}_x>0$, namely,

$$\mathcal{H}_s(\bar{y},\bar{p}_y;E_n) = \mathcal{H}(0,\bar{y},P_x^+(0,\bar{y},\bar{p}_y;E_n),\bar{p}_y), \tag{8}$$

where $P_x^+(0,\bar{y},\bar{p}_y;E_n)$ is the positive classical momentum in x coordinate obtained from the Hamiltonian function at the surface of section, that is,

$$P_x^+(0,y,p_y;E) = +\left[2E - p_y^2 - y^2\left(\omega^2 - \tfrac{2}{3}\lambda y\right)\right]^{1/2}. \tag{9}$$

The zeros of the QPSS $\mathcal{H}_s(\bar{y},\bar{p}_y)$ have been computed by using the properties of the *index* of a curve [26]. Let $\mathcal{T}:\mathbf{x}\mapsto\mathbf{x}'$ be a continuous transformation $\mathbb{R}^2\xrightarrow{\mathcal{T}}\mathbb{R}^2$, then the index of a closed curve defined in the source space $\mathbf{x}$ equals the number of zeros in the target space $\mathbf{x}'$ enclosed by that curve. Moreover, the index of a curve is the winding number of the transformed curve around the coordinate origin of the target space. Thus, taking into account that the Husimi QPSS, same as the Husimi function, is the squared modulus of a complex number z, i.e.,

$$\mathcal{H}_s(\bar{y},\bar{p}_y) = (\mathrm{Re}^2(z)+\mathrm{Im}^2(z)), \tag{10}$$

the transformation

$$\mathcal{T}:(\bar{y},\bar{p}_y)\mapsto(\mathrm{Re}(z),\mathrm{Im}(z)) \tag{11}$$

has been considered. Then, the source space $(\bar{y},\bar{p}_y)$ has been divided into square cells, and the number of zeros contained in each cell numerically calculated by counting the winding number of the transformed cell in the target space $(\mathrm{Re}(z),\mathrm{Im}(z))$.

Finally, it is interesting to note that by using the Gaussian basis set defined in Eq. (4), the integrals involved in the calculation of the matrix representation of the Hamiltonian operator, and also in the basis set change in Eq. (6), are analytic, so that there are no further numerical approximations in our calculations than the finite size of the basis set.

III. RESULTS AND DISCUSSION

A. Classical dynamics

The classical behavior of the bounded region of the Hénon-Heiles system, as total energy increases, is summarized in Fig. 2, where the corresponding composite PSSs for the escape energy $E_s=9.524$ and also for $3E_s/4$, $E_s/2$, and $E_s/4$ are shown.

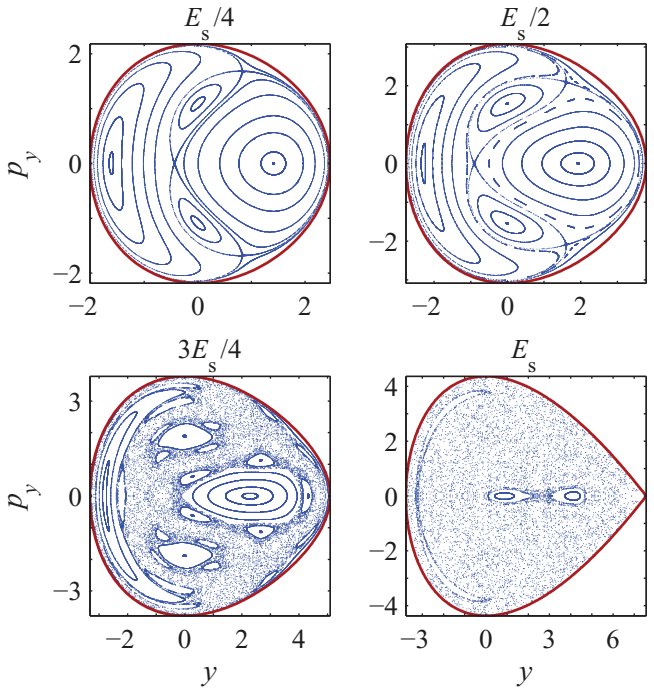

FIG. 2. (Color online) Composite Poincaré surfaces of section, with $x=0$ and $p_x>0$, of the bounded region of the Hénon-Heiles system depicted in Fig. 1 for total energies $E_s/4$ (top left), $E_s/2$ (top right), $3E_s/4$ (bottom left), and E_s (bottom right), where $E_s=9.524$ is the escape energy.

At energy $E_s/4$ the system is completely regular, with a very simple phase space structure. As can be seen in top left panel of Fig. 2, there are two principal tori families, around the two elliptic fixed points with $p_y=0$ (rotations), separated by a chain of islands (librations). The two rotation POs have the same graph in configuration space (x,y), a closed curve traveled clockwise or counterclockwise. Consequently, both principal tori families are topologically equivalent. Observe that, as is clear from the canonical transformation to polar coordinates in Eq. (2), the angular momentum p_θ for the rotation POs at the PSS, where $x=p_y=0$, fulfills $p_\theta>0$ (counterclockwise) for the fixed point with $y<0$ and $p_\theta<0$ (clockwise) for $y>0$. Moreover, the two libration POs corresponding to the elliptic fixed points in the chain of islands are contained in the symmetry planes σ_2 (for the fixed point with $p_y>0$) and σ_3 (for $p_y<0$). Notice that the angular momentum for these POs at the PSS, where $x=y=0$, is $p_\theta=0$. There is a third PO contained in the symmetry plane σ_1 but, as was pointed out in Sec. II B, the corresponding fixed point is degenerate over the energy boundary. Lastly, the three libration PO's corresponding to the hyperbolic fixed points in the chain of islands have a "smile"-shaped graph in configuration space for the fixed point with $p_y=0$, and the C_3 symmetry rotations of the smile-shaped graph for the other two fixed points.

For energy $E_s/2$ the phase space structure remains very regular, although some new chains of islands have appeared,

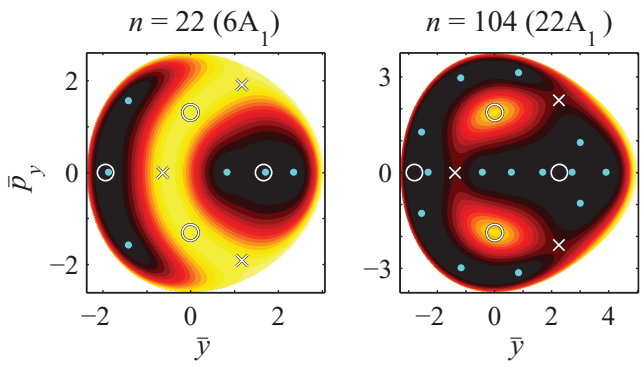

FIG. 3. (Color online) Quantum Poincaré surfaces of section based on the Husimi function, with $\bar{x} = 0$ and $\bar{p}_x > 0$, corresponding to two characteristic samples of the quasibounded nondegenerate eigenstates A_1 of the Hénon-Heiles system. Eigenstates $6A_1$ (left) and $22A_1$ (right) have their eigenenergies $E_n = 3.410, 7.040$, respectively, below and above the classical order-chaos threshold energy $E_b = 4.762$. Minima and maxima are represented, respectively, as darker and lighter regions in the color scale, the zeros being marked with filled circles (•). Also, the principal fixed points for each eigenenergy have been superimposed as open circles (◯) and crosses (×), corresponding, respectively, to the elliptic and hyperbolic fixed points.

and also a very thin stochastic band around the separatrix related to the smile-shaped POs is present. Notice that, as was shown by Toda [23], $E_b = E_s/2 = 4.762$ corresponds to the energy threshold in the order-chaos transition.

At energy $3E_s/4$ the system has a mixed phase space with regular regions (tori and chains of islands) and also chaotic regions. Finally, for the escape energy E_s chaos is fully developed, the two principal elliptic fixed points have suffered a pitchfork bifurcation becoming hyperbolic, and only two little islands arisen from each pitchfork bifurcation remain as regular structures in phase space.

B. Quantum eigenstates

The behavior of the distributions of zeros of the Husimi function for the nondegenerate energy eigenstates is the expected one, i.e., the distributions are one dimensional for states below the classical order-chaos threshold energy E_b and they are basically two-dimensional for states above it.

In Fig. 3 the distributions of Husimi zeros for two samples of nondegenerate states below $(6A_1)$ and above $(22A_1)$ the classical threshold energy E_b are depicted. Observe that state $6A_1$ has the Husimi zeros distributed along the line $\bar{p}_y = 0$ around the principal elliptic point with $\bar{y} > 0$, and along a cross line around the principal elliptic point with $\bar{y} < 0$. As energy increases, new Husimi zeros are located in the same manner as state $6A_1$. However, beyond threshold energy E_b some zeros break this one-dimensional pattern. Thus, state $22A_1$ has two zeros around the principal elliptic point $\bar{y} > 0$ located perpendicular to line $\bar{p}_y = 0$, leading to a two-dimensional distribution.

We have verified that, as chaos parameter λ tends to zero, some A_1 nondegenerate energy eigenstates tend to the angular momentum $\widehat{P}_\theta$ (and energy) eigenstates of the isotropic harmonic oscillator, so that it is possible to assign the corresponding quantum numbers to the states at $\lambda = \sqrt{0.0175}$. Thereby, the states $6A_1$ and $22A_1$ in Fig. 3 correspond to three and seven, respectively, radial excitations and null angular excitations. Note that the irregular state $22A_1$ is clearly localized on the POs contained in the three symmetry planes σ_i $(i = 1,2,3)$. Due to the symmetry of the system, when the number of angular excitations is a multiple of 3, the nondegenerate energy eigenstates do not correspond to angular momentum eigenstates but they correspond to sum and difference combinations of angular momentum eigenstates, resulting in a pair (A_1, A_2) of nondegenerate states with very close eigenenergies. In this case, the Husimi zeros are distributed around the principal chain of islands instead of around the two principal tori families.

On the other hand, the behavior of the distribution of Husimi zeros for the degenerate eigenstates E is not clear. As shown in Fig. 4, where three samples of degenerate states below $(6E)$, similar $(17E)$, and above $(42E)$ the classical threshold energy E_b are represented, the distributions are apparently two dimensional and without a clear pattern in all three cases.

However, due to the degeneracy, the pairs of eigenstates E shown in Fig. 4 can be linearly combined to obtain different pairs of eigenstates E, with the same eigenenergies but different distributions of Husimi zeros. Namely, these pairs of degenerate eigenstates come directly from the diagonalization procedure, and hence they do not necessarily characterize the degree of chaos in the system. We should search for linear combinations that have an approximate second constant of motion (in addition to energy). Considering the behavior of the nondegenerate eigenstates as the chaos parameter λ tends to zero described above, the angular momentum $\widehat{P}_\theta$ sounds a reasonable choice for the approximate second constant of motion.

Thus, the orthogonal transformation of each pair of real degenerate eigenstates $(|n_1\rangle, |n_2\rangle)$, obtained directly from the diagonalization procedure, have been regarded

$$\begin{pmatrix} |n_1'\rangle \\ |n_2'\rangle \end{pmatrix} = \begin{pmatrix} \cos\vartheta & \sin\vartheta \\ -\sin\vartheta & \cos\vartheta \end{pmatrix} \begin{pmatrix} |n_1\rangle \\ |n_2\rangle \end{pmatrix}, \tag{12}$$

where $0 \leqslant \vartheta \leqslant \frac{\pi}{2}$, and the angular momentum uncertainty $\Delta\widehat{P}_\theta$ for the resulting eigenstates $(|n_1'\rangle, |n_2'\rangle)$ calculated as a function of mixing angle ϑ. Curiously, the uncertainty $\Delta\widehat{P}_\theta$ does not depend on mixing angle ϑ.

Nevertheless, we are not taking into account all possible linear combinations. The Hilbert space of quantum mechanics is, in general, not real but complex. Therefore, the most general transformation to be regarded is not the orthogonal transformation but the unitary transformation

$$\begin{pmatrix} |n_1'\rangle \\ |n_2'\rangle \end{pmatrix} = \begin{pmatrix} \cos\frac{\vartheta}{2} & e^{i\eta}\sin\frac{\vartheta}{2} \\ -e^{-i\eta}\sin\frac{\vartheta}{2} & \cos\frac{\vartheta}{2} \end{pmatrix} \begin{pmatrix} |n_1\rangle \\ |n_2\rangle \end{pmatrix}, \tag{13}$$

where $0 \leqslant \vartheta \leqslant \pi$ and $0 \leqslant \eta < 2\pi$. By using the unitary transformation, the angular momentum uncertainty for the resulting eigenstates is really a function of both mixing angles, ϑ and η, as shown in Fig. 5. Mixing angles define a sphere of unit radius, the so called Bloch sphere, where opposite points represent orthonormal vectors. In Fig. 5 the Bloch sphere has been represented as a rectangle, so that left and right sides are

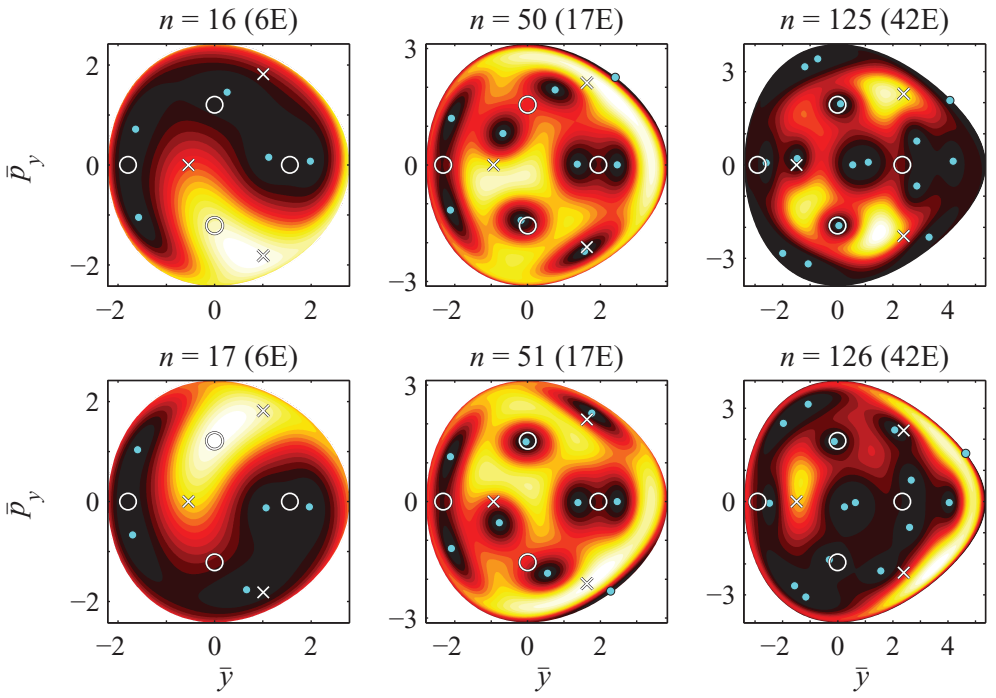

FIG. 4. (Color online) Same as described in the caption of Fig. 3 for three characteristic samples of the quasibounded degenerate eigenstates E of the Hénon-Heiles system obtained directly from the diagonalization procedure. Eigenstates $6E$ (left), $17E$ (middle), and $42E$ (right) have their eigenenergies $E_n = 2.937, 4.875, 7.573$, respectively, below, similar, and above the classical order-chaos threshold energy $E_b = 4.762$.

the same, the top side collapses into a point corresponding to the nadir of the sphere, and the bottom side collapses into a point corresponding to the zenith (standard orientation). Observe that meridians $\eta = 0$ and $\eta = \pi$ divide the sphere in two symmetric parts, where the points $(\vartheta, \eta) = (\frac{\pi}{2}, \frac{\pi}{2})$ and $(\frac{\pi}{2}, \frac{3\pi}{2})$ represent the two orthonormal eigenstates with the same minimum uncertainty $\Delta\widehat{P}_\theta$. In addition, note that the orthogonal transformation in Eq. (12) corresponds to the unitary transformation along the meridian $\eta = 0$, where the uncertainty $\Delta\widehat{P}_\theta$ is maximum and constant, and also the resulting eigenstates remain real.

The Husimi QPSSs corresponding to the degenerate eigenstates $6E$, $17E$, and $42E$, with minimum uncertainty $\Delta\widehat{P}_\theta$, are represented in Fig. 6. Now, the behavior of the distributions of Husimi zeros is the expected one, similarly to the nondegenerate eigenstates case. Thus, the eigenstates $6E$, with eigenenergy below the classical threshold energy E_b, have their zeros aligned in one-dimensional distributions around both principal families of tori. In the case of the eigenstates $17E$ whose eigenenergy is similar to, albeit above, the threshold energy, the Husimi zeros are beginning to spread out. Finally, the eigenstates $42E$, with eigenenergy well above the classical threshold energy, have their zeros clearly spread, leading to a two-dimensional distribution.

Notice that the pairs of degenerate eigenstates with minimum uncertainty $\Delta\widehat{P}_\theta$ correspond to states with expectation value of angular momentum given by $\langle n'|\widehat{P}_\theta|n'\rangle = (n^+ - n^-)\hbar$, where n^- and n^+ are the number of Husimi zeros around the two principal elliptic points at $p_y = 0$ with $y < 0$ and $y > 0$, respectively. Thus, states $6E$ in Fig. 6 have expectation

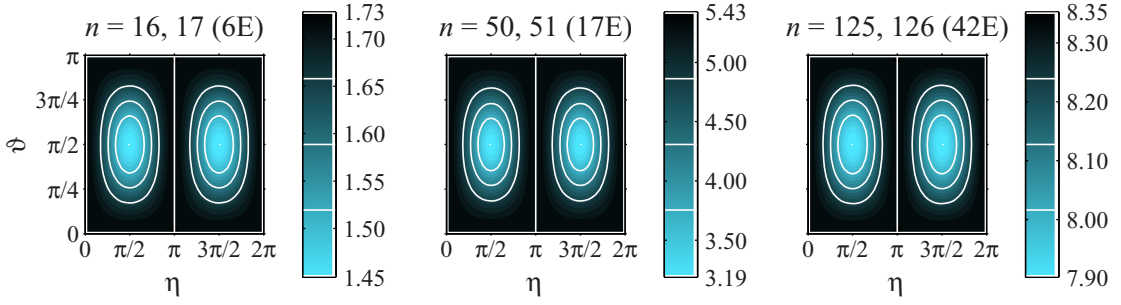

FIG. 5. (Color online) Standard deviation of angular momentum in Planck's constant units $\Delta\widehat{P}_\theta/\hbar$ over the Bloch sphere, corresponding to the unitary transformation of the degenerate eigenstates $6E$ (left), $17E$ (middle), and $42E$ (right). The color scale has been adjusted between minimum and maximum value for each case. In addition, equally spaced contour lines from the minimum to the maximum value, both included, have been superimposed on the figures and also on the color bars.

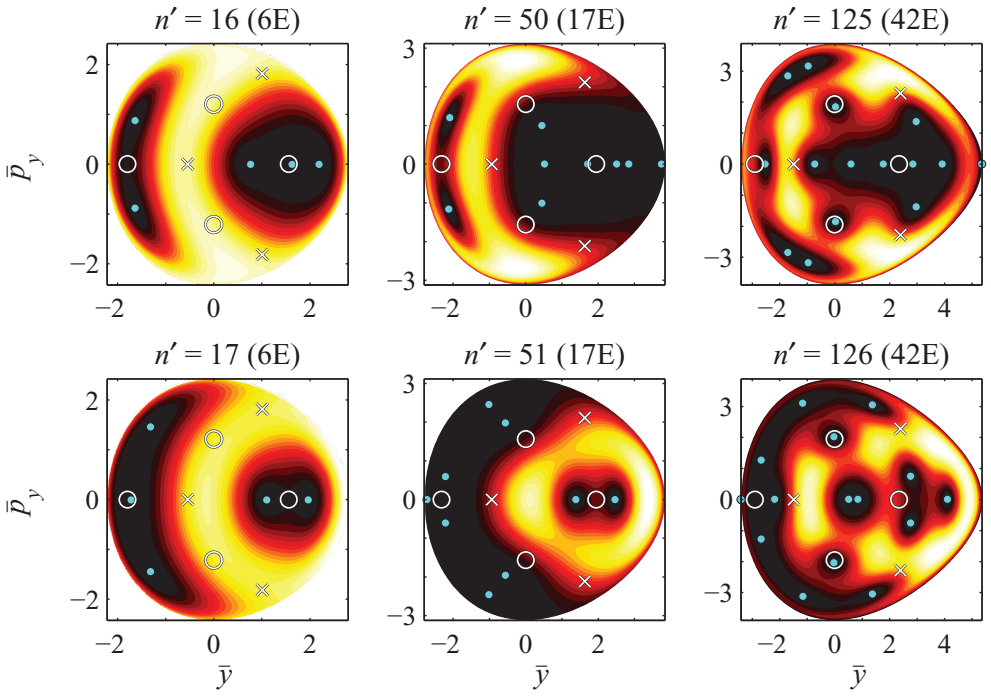

FIG. 6. (Color online) Same as described in the caption of Fig. 3 for the unitary transformation of the degenerate eigenstates $6E$ (left), $17E$ (middle), and $42E$ (right), shown in Fig. 4, corresponding to the minimum standard deviation of angular momentum.

value $\langle \widehat{P}_\theta \rangle = \pm\hbar$, states $17E$ have $\langle \widehat{P}_\theta \rangle = \pm 5\hbar$, and states $42E$ also have $\langle \widehat{P}_\theta \rangle = \pm 5\hbar$, albeit in the latter case, due to the spreading of zeros, the assignment of zeros to n^- or n^+ is not clear. Accordingly, at the integrable limit $\lambda \to 0$ minimum uncertainty states $6E$ correspond to two radial excitations and one angular excitation, states $17E$ correspond to two radial excitations and five angular excitations, and states $42E$ correspond to five radial excitations and also five angular excitations.

IV. CONCLUDING REMARKS

The distribution of zeros of the Husimi function of energy eigenstates has proven to be a useful tool for the characterization of quantum transition from order to chaos in systems with nondegenerate eigenstates [1–16].

We have studied the behavior of the distributions of Husimi zeros for systems with degeneracy by means of calculations on a QPSS of the Hénon-Heiles Hamiltonian system, whose potential energy function belongs to the C_{3v} symmetry point group, with two nondegenerate irreducible representations (A_1 and A_2) and a doubly degenerate one (E).

For the nondegenerate energy eigenstates, the distributions of Husimi zeros behave as expected: They are one dimensional for states below the classical order-chaos threshold energy and they are two dimensional for states above it.

For the doubly degenerate states, however, we have shown that it is necessary to consider a quantum observable for an approximate second constant of motion (the angular momentum, in our case), and obtain the linear combination of degenerate states with minimum uncertainty in this quantum observable. In this way, the distributions of Husimi zeros of the degenerate states behave as in the nondegenerate case.

Finally, it should be noted that the linear combination of degenerate states should be the most general unitary transformation rather than the standard orthogonal transformation, particularly when the observable corresponding to the approximate second constant of motion has complex eigenstates (as it is in our case with the angular momentum).

ACKNOWLEDGMENT

This research was supported by the Ministry of Economy and Competitiveness–Spain under Grant No. MTM2012-39101.

[1] P. Leboeuf and A. Voros, J. Phys. A **23**, 1765 (1990).
[2] S. Nonnenmacher, Nonlinearity **10**, 1569 (1997).
[3] S. Nonnenmacher and A. Voros, J. Stat. Phys. **92**, 431 (1998).
[4] D. A. Wisniacki, M. Saraceno, F. J. Arranz, R. M. Benito, and F. Borondo, Phys. Rev. E **84**, 026206 (2011).
[5] M. B. Cibils, Y. Cuche, P. Leboeuf, and W. F. Wreszinski, Phys. Rev. A **46**, 4560 (1992).
[6] E. Romera, R. del Real, and M. Calixto, Phys. Rev. A **85**, 053831 (2012).
[7] J. M. Tualle and A. Voros, Chaos, Solitons Fractals **5**, 1085 (1995).

[8] D. Biswas and S. Sinha, Phys. Rev. E **60**, 408 (1999).
[9] H. J. Korsch, C. Müller, and H. Wiescher, J. Phys. A **30**, L677 (1997).
[10] F. Toscano and A. M. O. de Almeida, J. Phys. A **32**, 6321 (1999).
[11] J. P. Amiet and S. Weigert, J. Opt. B **1**, L5 (1999).
[12] L. E. Konkov, D. V. Makarov, E. V. Sosedko, and M. Y. Uleysky, Phys. Rev. E **76**, 056212 (2007).
[13] F. J. Arranz, F. Borondo, and R. M. Benito, Phys. Rev. Lett. **80**, 944 (1998).
[14] F. J. Arranz, R. M. Benito, and F. Borondo, J. Chem. Phys. **123**, 044301 (2005).
[15] F. J. Arranz, Z. S. Safi, R. M. Benito, and F. Borondo, Eur. Phys. J. D **60**, 279 (2010).
[16] F. J. Arranz, L. Seidel, C. G. Giralda, R. M. Benito, and F. Borondo, Phys. Rev. E **87**, 062901 (2013).
[17] M. Hénon and C. Heiles, Astron. J. **69**, 73 (1964).
[18] C. Manchein and M. W. Beims, Phys. Lett. A **377**, 789 (2013).
[19] G. Saxena, A. Prasad, and R. Ramaswamy, Phys. Rev. E **87**, 052912 (2013).
[20] H. A. Posch, J. Phys. A **46**, 254006 (2013).
[21] J. D. Bernal, J. M. Seoane, and M. A. F. Sanjuán, Phys. Rev. E **88**, 032914 (2013).
[22] M. Avendaño-Camacho, J. A. Vallejo, and Y. Vorobjev, J. Phys. A **46**, 395201 (2013).
[23] M. Toda, Phys. Lett. A **48**, 335 (1974).
[24] I. P. Hamilton and J. C. Light, J. Chem. Phys. **84**, 306 (1986).
[25] E. Anderson, Z. Bai, C. Bischof, S. Blackford, J. Demmel, J. Dongarra, J. Du Croz, A. Greenbaum, S. Hammarling, A. McKenney, and D. Sorensen, *LAPACK User's Guide* (SIAM, Philadelphia, 1999).
[26] V. I. Arnold, *Ordinary Differential Equations* (Springer-Verlag, Berlin, 1992).